Available online at www.sciencedirect.com
SCIENCE DIRECT
International Journal of Heat and Mass Transfer 49 (2006) 159–170
International Journal of HEAT and MASS TRANSFER
www.elsevier.com/locate/ijhmt

Measurement of detailed heat transfer along rib-roughened surface under arrays of impinging elliptic jets

W.M. Yan *, S.C. Mei

Department of Mechatronic Engineering, Huafan University, Shih Ting, Taipei 22305, Taiwan, ROC

Received 20 May 2005; received in revised form 15 July 2005
Available online 5 October 2005

Abstract

The objective of the present study is to examine the detailed heat transfer coefficient distributions over a ribbed-surface under impingement of elliptic jet arrays using a liquid crystal thermograph technique. Both continuous and broken V-shaped-rib configurations with different exit flow orientations were considered. To examine the angled rib effects, three angled ribs were discussed under jet-to-plate spacing $Z = 3$ for different Reynolds numbers. Measured results show that the local heat transfer rates over the ribbed-surface are characterized by obvious periodic-type variation of Nusselt number distributions. The downstream peaks are diminished for increasing crossflow effect. Compared to the results without ribs, the heat transfer over the ribbed-surface may be enhanced or retarded. Whereas, among the test angled-rib arrangements, the best heat transfer performance is obtained with a surface with 45° V-shape ribs. In addition, the surface with continuous ribs provides a better impingement heat transfer than that with broken ribs.
© 2005 Elsevier Ltd. All rights reserved.

1. Introduction

The characteristics of fluid flow and heat transfer of jet impingement over a ribbed-surface are very important and often encountered in a variety of practical applications, e.g., cooling of hot steel plate, gas turbine cooling, thermal management of microelectronic components, etc.

For jet array impingement heat transfer over a smooth wall, the geometric/thermo-fluid parameters, e.g., jet array pattern, Reynolds number, crossflow, jet-to-target distance and their coupling effects have a considerable impact on the characteristics of the fluid flow and heat transfer. The characteristics of fluid flow and heat transfer under an array of air impinging jets have been investigated in the open literature [1,2]. In recent years, many investigators [3,4] have examined the heat transfer characteristics of an array of liquid impinging jets. They focused mainly on the heat transfer under impinging jets for which crossflow effects, which potentially reduce the high stagnation heat transfer associated with impinging jets, are designed to be minimal.

Recently, the liquid crystal thermograph has been employed as a reliable temperature sensor to measure the local heat transfer coefficients. It has become a widely-used technique for its merits of whole surface heat transfer measurements. Detailed heat transfer distributions under arrays of jets impinging on a surface with dimpled or film hole surfaces were investigated by

* Corresponding author. Tel.: +886 2 26632102; fax: +886 2 26632143.
E-mail address: wmyan@huafan.hfu.edu.tw (W.M. Yan).

0017-9310/$ - see front matter © 2005 Elsevier Ltd. All rights reserved.
doi:10.1016/j.ijheatmasstransfer.2005.07.043

Nomenclature

AR	aspect ratio of elliptic jet hole
d	equivalent diameter of impinging elliptic jet port
h	local heat transfer coefficient, W/m^2 K
k	thermal conductivity of acrylic material, W/m K
k_f	air thermal conductivity, W/m K
Nu	Nusselt number, hd/k_f
Re	jet Reynolds number, Vd/v
T_i	initial temperature of the target surface, °C or K
T_∞	mainstream temperature of the air flow, °C or K
T_w	color change temperature of the liquid crystal, red-to-green, °C or K
t	transient test time, s
V	average velocity of impinging jet, m/s
X, x	dimensionless and dimensional axial distance of the target surface , $X = x/d$
Y, y	dimensionless and dimensional spanwise distance, $Y = y/d$
Z, z	dimensionless and dimensional spacing between jet plate and target plate, $Z = z/d$
Greek symbols	
α	thermal diffusivity of acrylic material, m^2/s
γ	dimensionless time variable defined in Eq. (2), $h\sqrt{\alpha t}/k$
v	kinematic viscosity of air, m^2/s
τ_j	time step, s

Treuren et al. [5], Huang et al. [6], Azad et al. [7], Rhee et al. [8] and Kanokjaruvijit and Martinez-botas [9]. The results revealed that the crossflow and the exit flow direction have a significantly impact on the heat transfer distributions on a target surface. Their results focused on the heat transfer under in-line arrays of jets impinging on a surface. Recently, also by using transient TLC techniques, Yan et al. [10] carried out a study on heat transfer enhancement over a base plate with obstacles effects. In addition, Yan et al. [11,12] performed experimentally a series of impinging heat transfer over a smooth surface under in-line and staggered jet arrays with circular or elliptic jet holes. However, the studies in the past are mostly on a flat surface with relatively few over a curved surface [13]. In a practical situation, the surface which needs to be cooled may not be smooth and may be roughened. In order to obtain augmented heat transfer, periodic ribs are often employed in the design of gas turbine engines and heat exchangers. An experimental study of impinging jet flow structure and heat transfer along the rib-roughened surface was examined by Gau and Lee [14]. In their study, a single jet flow is considered only. As for the study about rib turbulators on the heat transfer and pressure drop along a channel or a multipass channel, the effects of rib height, rib pitch, rib angle of attack, etc., on the heat transfer characteristics have investigated systematically by Han and co-workers [15–19]. More recently, Yan et al. [20], by using transient TLC techniques, reported the impinging heat transfer over a continuous ribbed-surface under a circular jet arrays.

However, the broken or V-shape broken ribbed-surface is also used in the application of heat transfer enhancement. In addition, the impingement heat transfer with elliptic jet arrays can provides a better heat transfer [12]. Therefore, the measurement of detailed heat transfer along the rib-roughened surface under arrays of impinging elliptic jets with continuous or broken ribs are examined in this work. The effects of continuous or broken rib configuration with different ribbed angles were explored. Besides, the effects of crossflow, exit flow orientation and jet Reynolds number are investigated. To resolve the highly localized heat transfer distributions, a transient liquid crystal technique in connection with a thin film of thermochromic liquid crystal (TLC) coated directly on the impingement target surface is used to measure the local heat transfer distributions. During a transient test, the color change of TLC film on the target surface was monitored and recorded by an automatic computer vision system and a data acquisition system. The time of color change of the liquid crystal to green is measured using an image processing equipment.

2. Experimental apparatus and procedure

Fig. 1 presents a schematic diagram of the experimental apparatus. The experimental apparatus consists of an image-processing system, a blower, an electric heater, a honeycomb set, a plenum, a computerized data acquisition system, and a test section. The test section consists of two compartments separated by a jet plate with an array of elliptic holes of hydraulic diameter $d = 10$ mm and aspect ratio AR $= 0.5$ on it. The top compartment is called pressure chamber, while the bottom compartment is the impingement channel. The airflow entering the pressure compartment goes downward to impinge the target plate through the elliptic holes. On the jet plate, 9 (streamwise) $\times$ 3 (spanwise) jet holes are arranged in an in-line pattern. The center-to-center dis-

tance between two neighboring jet holes are $3d$ and $1.5d$ in the streamwise and spanwise directions, respectively. The inlet pressure chamber has a cross-section of 100 mm × 50 mm.

The target plate is made of a black acrylic plate coated with liquid crystal on the inside surface. The target surface with rib arrangement is of 10 mm in thickness and 300 mm × 100 mm in area. The rib pitch, width and height are 60 mm, 5 mm and 2.5 mm, respectively. The choice of the black acrylic is due to its low thermal conductivity. The test section is assembled after a thin film of the liquid crystal (Hallcrest, BW/R38C5W/C17-10) sprayed uniformly on the target surface. The computerized data acquisition system consists of a digital image processing system and a data logger. The image processing system used in this work is composed of a digital color camcorder (camera + image recorder, SONY DCR-TRV7), a frame grabber card, and a Pentium IV personal computer. The isotherms of red-to-blue transition band were captured through a digital color camcorder with resolution of 682 × 492 pixels.

The test section is ready for running when the air fan is switched to the "ON" condition. Meanwhile, the data logger for temperature measurement and the image processing system are set to trigger for initiating data measurement at the same instant. The image processing system records the transition time for the color changing into green, and transmits the data into a matrix of the time for color-change over the entire test surface. The data of time and temperature are input to a computer program to determine the local heat transfer coefficients. Since the actual color image can be affected from many factors such as the thickness and surface condition of liquid crystal, the angle of camera and lighting illuminator, a careful temperature calibration of liquid crystal has to be done. The TLC and thermocouples with a FLUKE Helios Plus data logger were used. The liquid crystal was calibrated using the digital image processing system under the same conditions of experimental runs, including the illuminating light and the camera-viewing angle. The detailed test procedure can be found elsewhere [11,12,20].

3. Heat transfer theory

For the acrylic material used for model assembly, the heat penetrating depth into the plate over the time duration needed to complete one test run is less than the target plate thickness. In addition, it is expected that the lateral conduction in the plate have no significant effect on the local surface temperature response. The local surface temperature on the target plate is thus represented by the classical one-dimensional response of a semi-infinite medium to the sudden step application of a fluid flow at temperature T_∞. The surface temperature can be expressed as

$$(T_w - T_i)/(T_\infty - T_i) = 1 - \exp(\gamma^2)\mathrm{erfc}(\gamma) \quad (1)$$

where

$$\gamma = h\sqrt{\alpha t}/k \quad (2)$$

In the above, T_i represents the initial temperature of the test surface and the T_∞ stands for the jet flow temperature. The thermal diffusivity α and the thermal

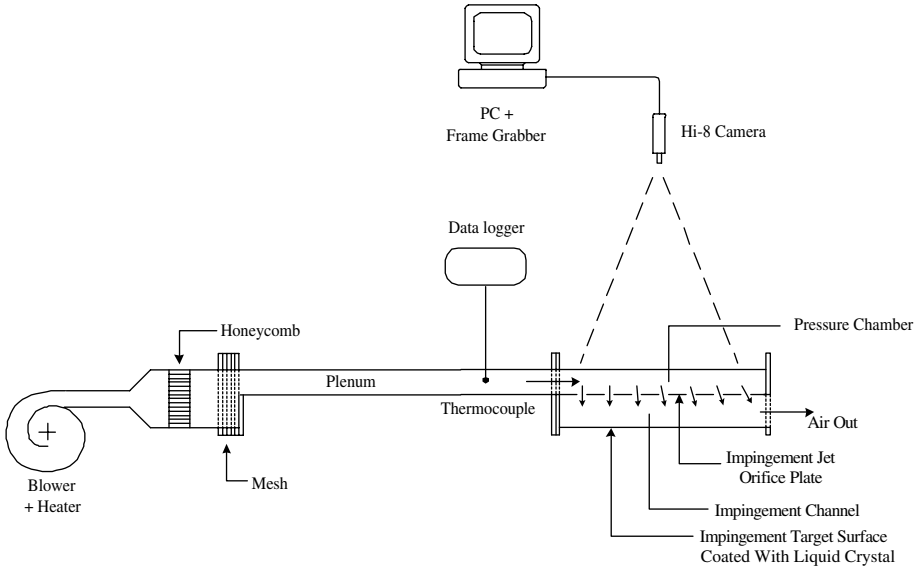

Fig. 1. Schematic diagram of the physical system.

conductivity k of the Acrylic material are known. To determine the local heat transfer coefficient h on the ribbed-surface, the temperature T_w for the color of the coated-surface turning into green was determined according to the calibration test of temperature change of the liquid crystal. The corresponding time, t, to reach the temperature for any surface is measured by using the image processing system. The time required for color change in a typical test run is about 15–90 s depending on the experimental conditions as well as the measurement locations.

In the present experimental runs, the target surface will not actually subjected to a step change in the driving air temperature due to the transient heating of the upstream jet plate and duct walls. Nevertheless, Eq. (1) is a fundamental solution that can be used to represent the response to a superposed set of gradual changes in T_∞. Using Duhamel's superposition theorem, the solution in Eq. (1) can be expressed as

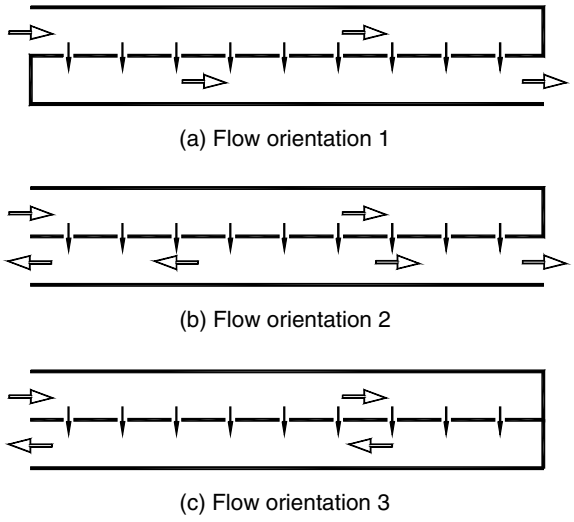

Fig. 2. Schematic diagram of the exit flow orientations.

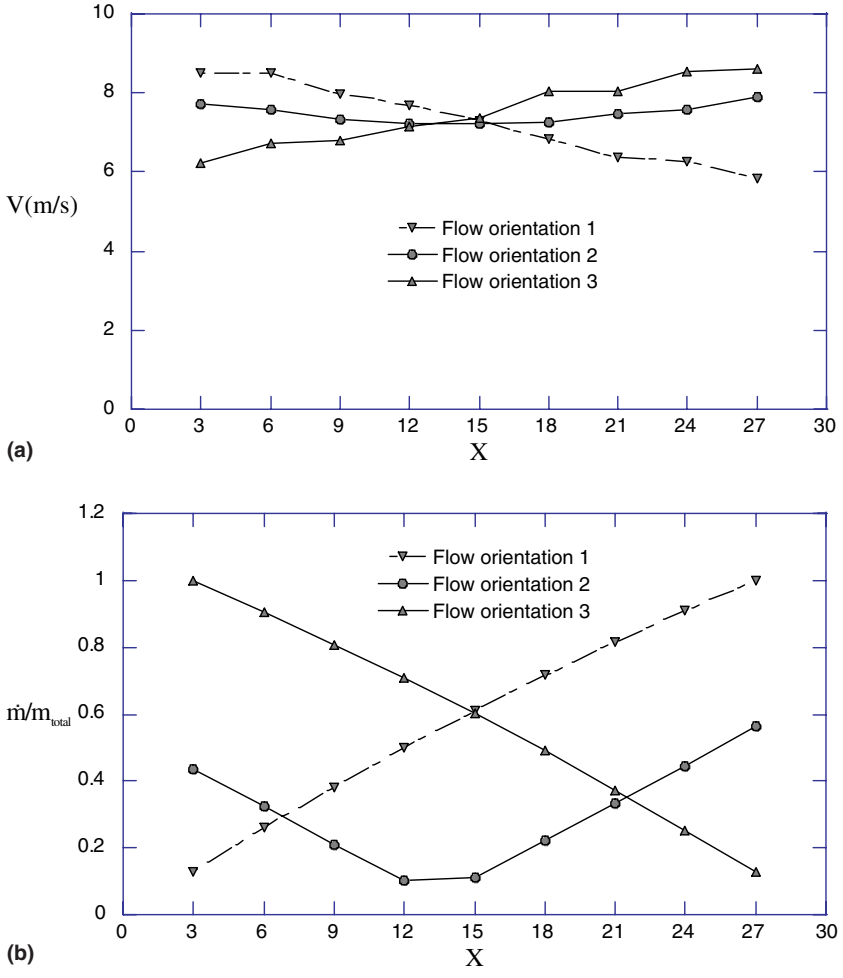

Fig. 3. Jet velocity and local mass flow rate along the channel axis for $Re = 3000$ and $Z = 3$.

$$T_w - T_i = \sum_{j=1}^{n} \left\{ 1 - \exp\left[\frac{h^2\alpha(t-\tau_j)}{k^2}\right] \operatorname{erfc}\left[\frac{h\sqrt{\alpha(t-\tau_j)}}{k}\right] \right\} [\Delta T_{\infty j}] \quad (3)$$

where ΔT_∞ and τ_j, respectively, are the flow temperature change and the time step from the recorder output of the jet flow temperature history. In the present work, the jet flow temperature T_∞ is determined by the thermocouple measurement in the pressure chamber prior to jet issue. The variation of T_∞ with time is recorded and approximated by step changes. With the color change time t at any location, the resulting superposed solution, Eq. (3), is used to solve for the local heat transfer coefficients on the target surface.

4. Results and discussion

4.1. Flow characteristics

For jet array impingement heat transfer over a ribbed-surface, the geometric/thermo-fluid parameters, e.g., jet array pattern, Reynolds number, crossflow, jet-to-target distance, angle-ribbed arrangements and their coupling effects have a considerable impact on the characteristics of the fluid flow and heat transfer. In this work, the emphasis is focused on the effects of angle-ribbed arrangements and jet-to-target spacing under different jet Reynolds numbers and spent-air crossflow orientations. To concentrated the effects of rib arrangements,

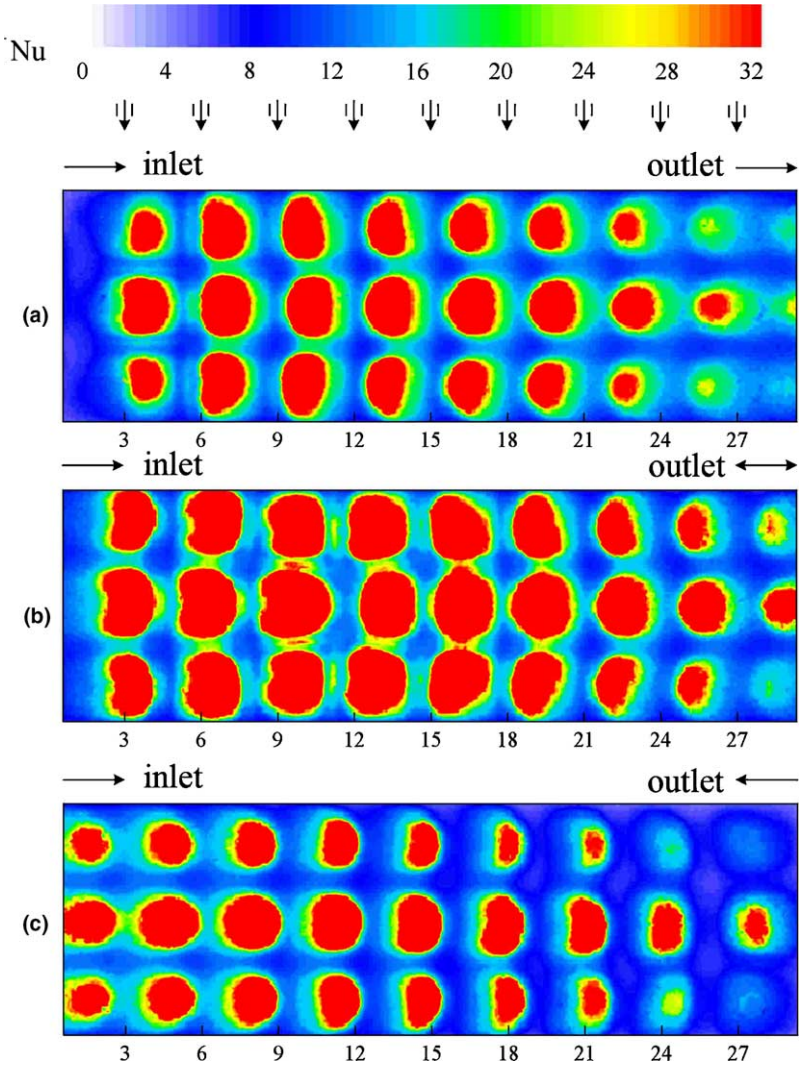

Fig. 4. Effects of flow orientation on local Nusselt number distributions on a smooth surface without ribs at $Re = 3000$, $Z = 3$, AR = 0.5 and flow orientations: (a) 1; (b) 2 and (c) 3.

the elliptic jet array with AR=0.5 are employed. Fig. 2 shows schematically three exit flow conditions designated as flow orientations 1, 2, and 3. The flow orientation 1 means that the flow first enters the pressure chamber from one end ($X = 0$) and, after ejected into the impingement channel, exits the impingement channel from the other end ($X = 30$). The flow enters and exits in the same direction. In the case with flow orientation 2, the flow enters the pressure chamber from $X = 0$ and exits the impingement channel from both ends ($X = 0$ and 30). For the flow orientation 3, the flow in the impingement channel exits in the opposite direction of the entry flow in the pressure chamber.

In the three cases mentioned above, the local mass flow rate is provided as one of the governing parameters, but the local jet velocity distribution along the channel axis is not controlled artificially. Therefore, it is very interesting as well as significant to understand the variation of the jet velocities from port to port along the longitudinal direction. For a typical case with $Re = 3000$, $Z = 3$ and AR = 0.5, Fig. 3(a) indicates the longitudinal variation of the spanwise average of jet velocity for elliptic jet arrays and Fig. 3(b) presents the corresponding local mass flow rate accumulated in the longitudinal (X) direction. Each local jet velocity is a transverse average of the three ports at each X-location at various conditions of exit flow. It is clearly found that the local velocities of both one-way exit cases, flow orientations 1 and 3, are nearly linear along X-direction and the maximum variations are around 30%. Whereas the jet velocity with the two-way exit, flow orientation 2, is nearly uniform with hole-to-hole variation about 15%. Due to

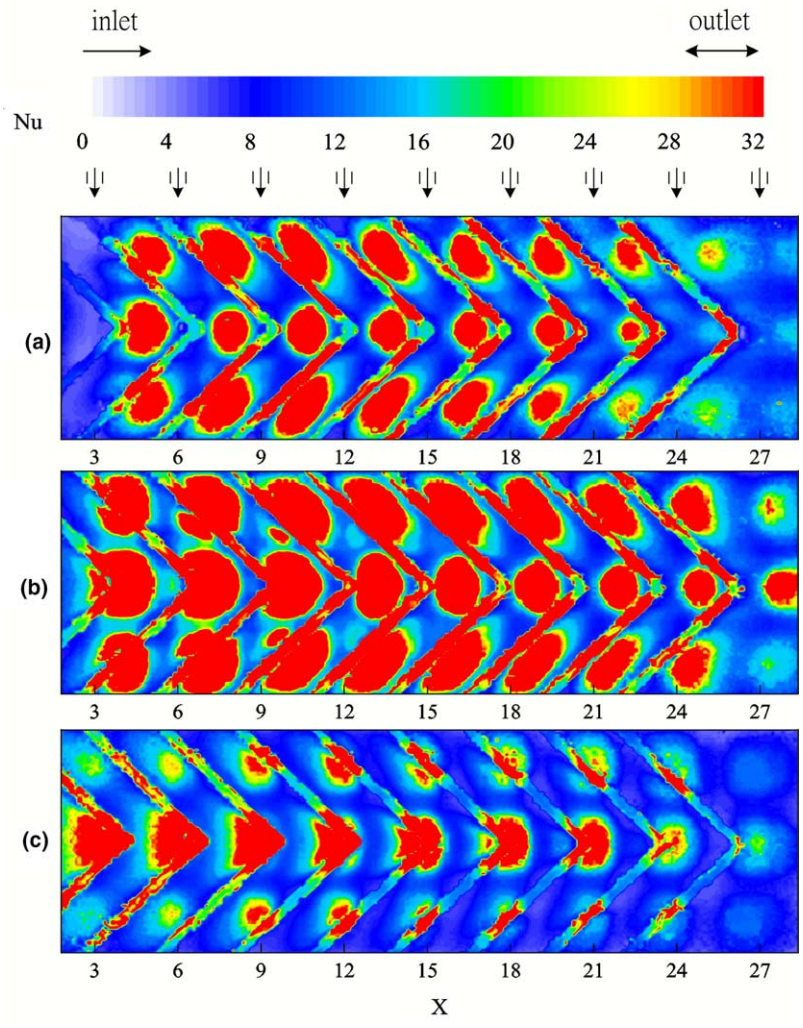

Fig. 5. Effects of flow orientation on local heat transfer distributions at $Re = 3000$, $Z = 3$, continuous ribbed-surface with 45° V-type ribs and flow orientations: (a) 1; (b) 2 and (c) 3.

the addition of the local jet flow, the mass flow rate is accumulated almost linearly along the main flow direction. The axial distribution of local mass flow rate in Fig. 3(b) is of a linearly increasing pattern from nearly center ($X = 12$–15) of the channel to the ends. The distribution of the local mass flow rate is a little asymmetric, which is attributed to the different left and right end conditions of the pressure channel. The left end of the pressure channel is an open inlet, while the right end is closed by a vertical end plate.

4.2. Liquid crystal thermographs of heat transfer rates

Fig. 4 shows the *Nu*-contours on a smooth surface at various exit conditions for $Re = 3000$ and $Z = 3$. The arrows in the figures with the abscissa $X = 3, 6, 9, \ldots, 27$ indicate the axial locations of the jet holes. The heat transfer performance is characterized by the Nusselt number defined as $Nu = hd/K_f$. Each spot in the thermographs shows the touchdown location and the shape of an impinging jet, where the heat transfer rate appearing as a peak due to the impingement effect. In each thermograph in Fig. 4, touchdown location of each elliptic jet has an obvious shift from the location of the jet hole. For the cases of flow orientation 1 in Fig. 4(a), in the upstream portion of the impingement channel where the crossflow is weak, the locations of the high-*Nu* spots deviate only slightly from the corresponding jet hole locations. As the crossflow develops, the locations of the heat transfer peaks are significantly shifted downstream. The extent of the touchdown location shift is more remarkable in the case of spent-air flow having the same direction as the flow in the pressure channel. The axial shift of the jet impingement location depends

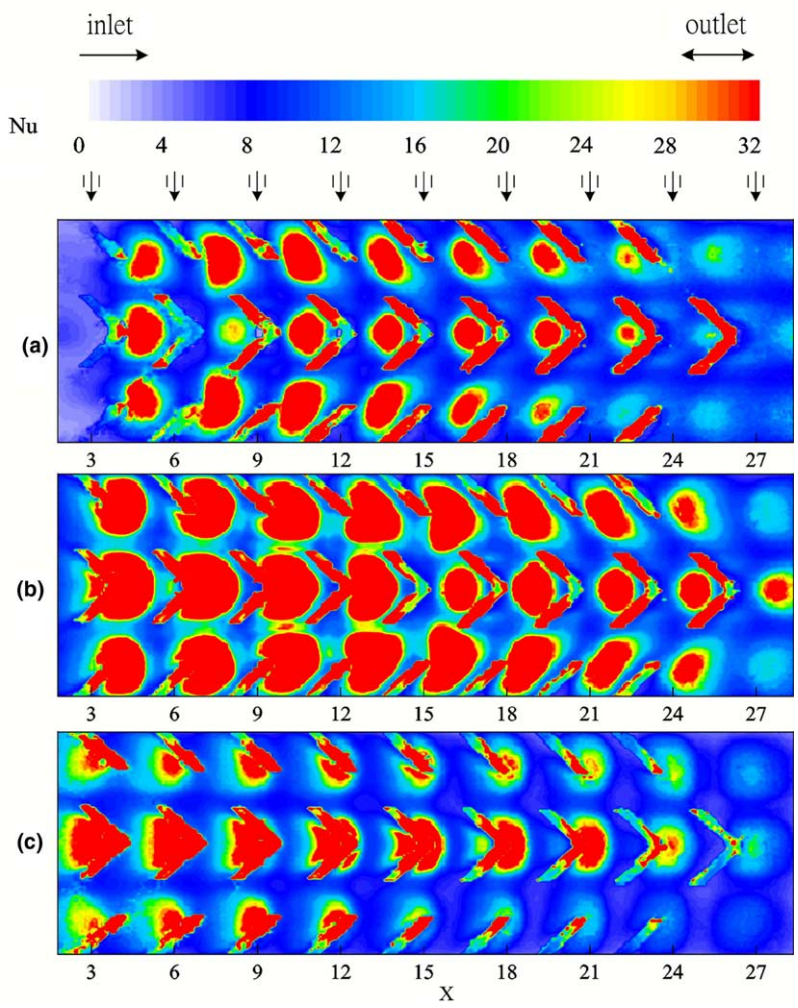

Fig. 6. Effects of flow orientation on local heat transfer distributions at $Re = 3000$, $Z = 3$, broken ribbed-surface with 45° V-type ribs and flow orientations: (a) 1; (b) 2 and (c) 3.

strongly on the axial momentum of the flow from the pressure channel. The extent of the touchdown location shift increases with an increase in the travel length of the crossflow, for which the stronger convection effect due to the accumulated flow in downstream part is the major reason. Accordingly, jets with the two-way exits, flow orientation 2, in Fig. 4(b) has relatively small shift. For the flow orientation3 in Fig. 4(c), the flow enters the pressure channel at $X = 0$ and, after turning to go through the jet holes and impinging the target plate, exits the impingement channel at $X = 0$ along the opposite direction. Due to the crossflow effect, the axial distributions of the spanwise average Nu show a shift of the impingement location toward the exit direction ($X = 0$). The extent of the shift is more significant near the exit end ($X = 0$) due to the stronger crossflow effects.

In Fig. 4, due to different crossflow effects, the distributions of the impinging spots and their shapes in the cases with three exit flow orientations are obviously different. In the case of flow orientation 2, relatively, the jet impinging effect performs the highest heat transfer rates among the three exit flow conditions, since in the latter case all the spent air exits from the channel center towards both ends and thus the heat transfer deterioration due to the crossflow effect is smallest.

Figs. 5 and 6 present the results of the effects of flow orientation on the local heat transfer distributions at $Re = 3000$ and $Z = 3$ over a continuous 45° V-type ribbed-surface and a broken 45° V-type ribbed-surface, respectively. By comparing Figs. 5 and 6, it indicates that the effects of the flow orientation on the distributions of the local Nusselt number over a roughened-sur-

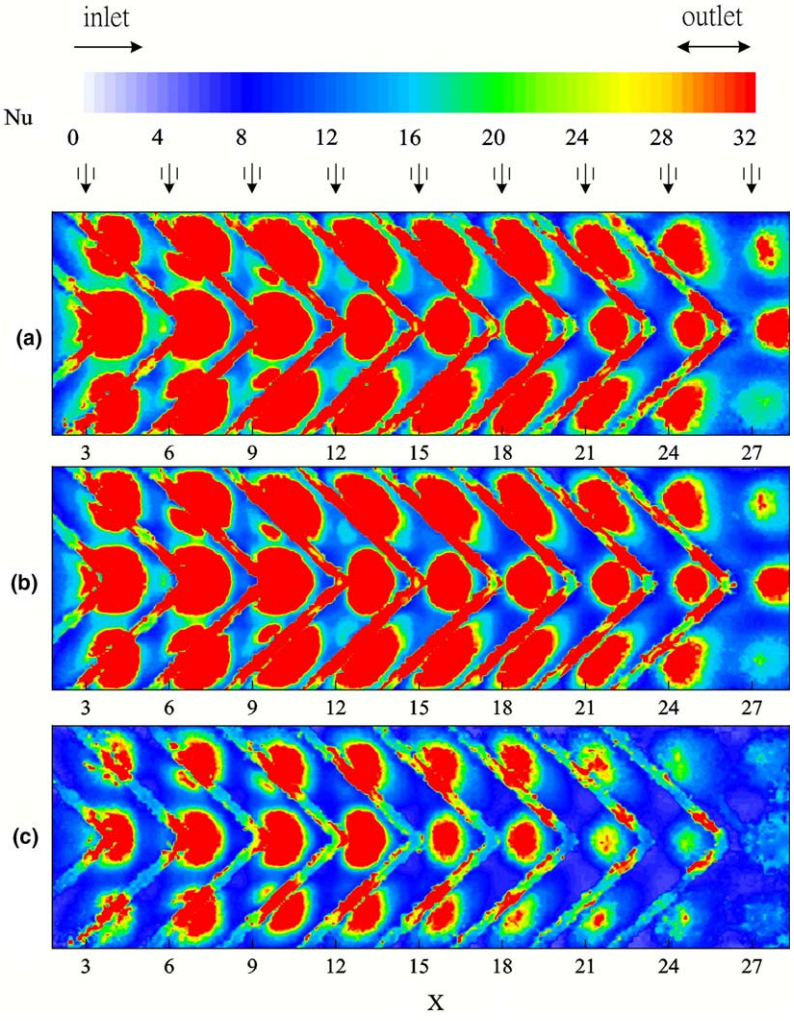

Fig. 7. Effects of Reynolds number on local heat transfer distributions at $Z = 3$, flow orientation 2, continuous ribbed-surface with 45° V-type ribs and jet Reynolds number: (a) 4500; (b) 3000 and (c) 1500.

face are similar to those over a smooth surface. But a careful examination of Figs. 5 and 6 discloses that better heat transfer performance is noted for the roughened-surface with continuous 45° V-type ribs.

For the study of internal cooling of turbomachinery, the information of jet impingement heat transfer with different jet Reynolds number is important to the related designer. Therefore, it is interesting to examine the effects of jet Reynolds number *Re* on the impingement heat transfer. Figs. 7 and 8 show the effects of jet Reynolds number *Re* on the detailed heat transfer coefficients over a continuous 45° V-type ribbed-surface and a broken 45° V-type ribbed-surface, respectively. In Fig. 7 or Fig. 8, the subplots (a), (b) and (c) correspond to the cases with $Re = 4500$, 3000 and 1500, respectively. The results show that the local heat transfer coefficient depends on the jet Reynolds number *Re*. As expected, the impinging force on the target surface is stronger for a higher jet Reynolds number *Re*. Therefore, larger Nu distributions are found for a higher *Re*. This confirms the concept that for convective heat transfer, better heat transfer is noted for a case with a higher Reynolds number. Like the results in Fig. 4, the local Nusselt numbers decreases as the spent air exits toward both ends ($X = 0$ and 30).

To enhance the heat exchange between the fluids and the solid, ribs are usually mounted on the heat transfer surface. But for the inappropriate rib arrangement, the presence of the ribs may retard the flow motion and the heat transfer. Therefore, the geometric arrangement of the ribs can be one of the significant factors. In Figs. 9 and 10, with the exit flow orientation 2, present the

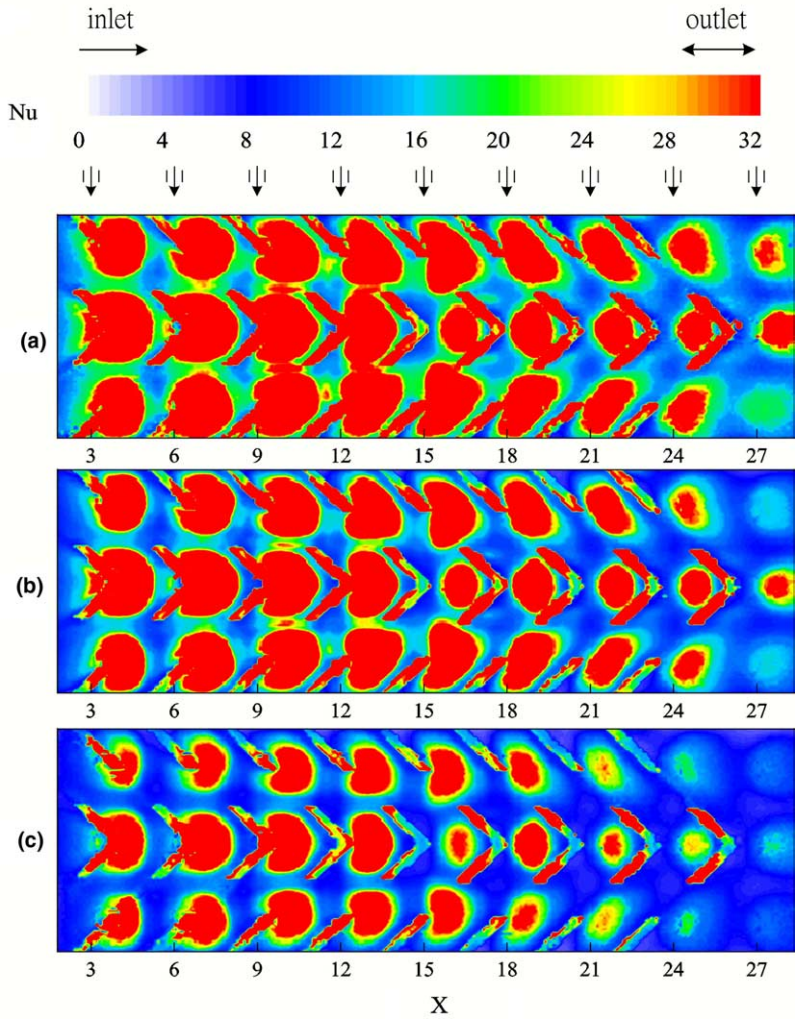

Fig. 8. Effects of Reynolds number on local heat transfer distributions at $Z = 3$, flow orientation 2, broken ribbed-surface with 45° V-type ribs and jet Reynolds number: (a) 4500; (b) 3000 and (c) 1500.

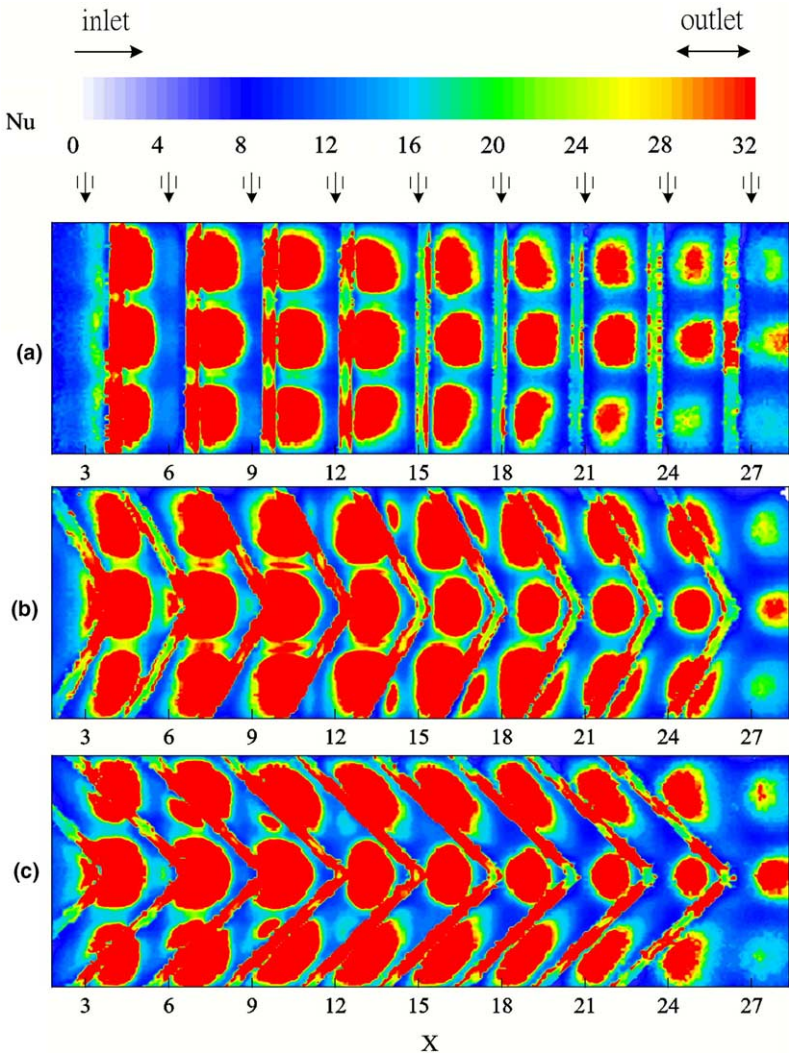

Fig. 9. Effects of rib angle on local heat transfer distributions over continuous ribbed-surface at $Re = 3000$, $Z = 3$, flow orientation 2 and rib angle of: (a) 90°; (b) 60° and (c) 45°.

rib-angle effects on the local heat transfer distributions over the continuous and broken ribbed-surfaces, respectively. In the case of 90° rib angle, see Fig. 9(a) or Fig. 10(a), the ribs just lie beneath the spanwise row of jet ports and impinged by the jets directly. It is observed in Fig. 9(a) or Fig. 10(a) that on the top of the rib the high heat transfer rate occurs. Comparing Fig. 9(a)–(c), the effects of rib-angle can be revealed. The heat transfer performance of 60° rib arrangement seems only to be similar to that of 90° one. But, relatively, the 45° ribs result in a very strong heat transfer enhancement over the whole assembly of base plate and ribs. It is believed that the favorable vortical flow structure stemming from the appropriate sweep angle of the ribs is the major reason. From the *Nu*-contours on the rib top surface in Fig. 9(c), appearance of swept vortical flows along the ribs can be inferred, and the vortices enhance the heat exchange between fluids and the solid boundaries. Comparison of the corresponding results between Figs. 9 and 10 indicates that a better heat transfer performance is noted for the roughened surface with continuous ribs. For numerical comparison of the effects of the angled-rib arrangement on the jet impingement on the continuous or broken ribbed-surface, Table 1 shows the averaged Nusselt number for different angled-rib arrangements. In addition, the averaged Nusselt number over a smooth surface ($\overline{Nu} = 37.88$) is also presented. It is clearly found in Table 1 that both the heat transfer on the continuous and broken ribbed-surfaces with 90° ribbed angle is smaller than that on the smooth surface.

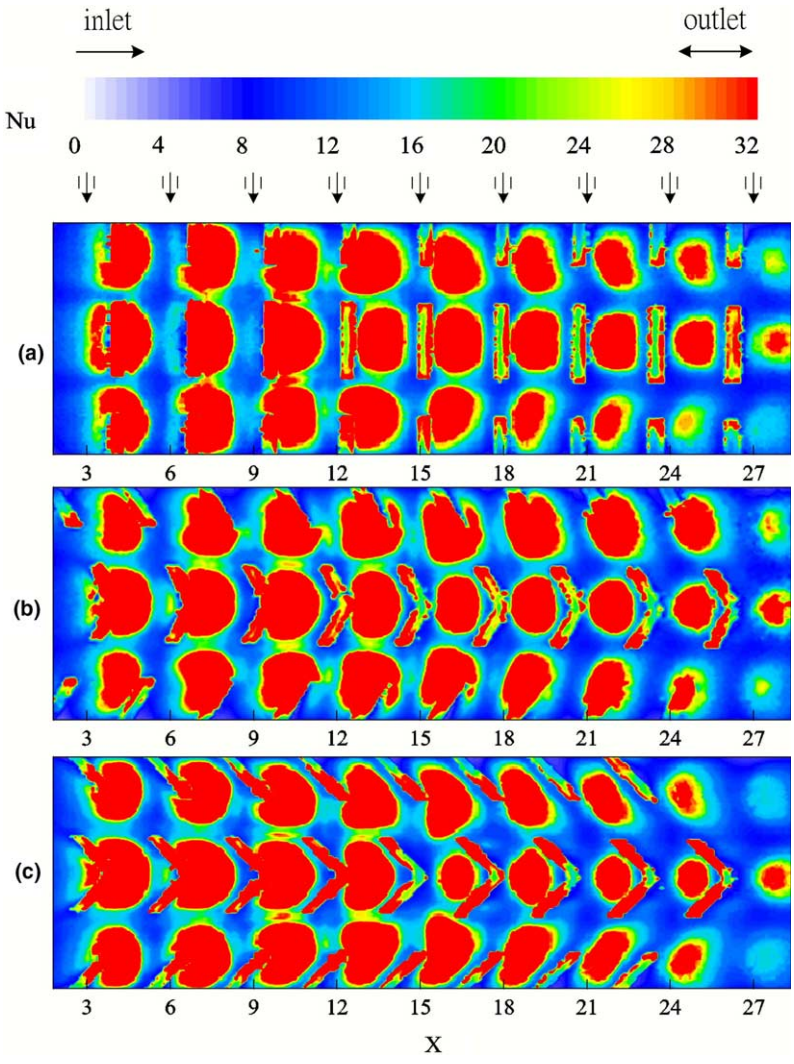

Fig. 10. Effects of rib angle on local heat transfer distributions over broken ribbed-surface at $Re = 3000$, $Z = 3$, flow orientation 2 and rib angle of: (a) 90°; (b) 60° and (c) 45°.

Table 1
Effects of rib arrangements on the averaged Nusselt number $\overline{Nu}$ of elliptic jet array impingement on ribbed-surface for $Re = 3000$, flow orientation 2, AR = 0.5 and $Z = 3$

Rib type	Rib angle		
	90°	60°	45°
Continuous ribs	33.948	38.236	45.741
Broken ribs	30.732	37.164	38.594

The averaged Nusselt number for elliptic jet array impingement heat transfer on smooth surface is $\overline{Nu} = 37.88$ [12].

But for the 45° rib arrangement, the impingement heat transfer is better than that on the smooth wall for both roughed surfaces with continuous and broken ribs. But for the 60° V-type ribbed-surface, the continuous ribbed-surface experiences a better heat transfer than that on the smooth surface. While for the broken ribbed-surface, the appearance of the broken ribs causes a decrease in the heat transfer, relatively to the smooth surface.

5. Conclusion

The detailed local heat transfer rates on a ribbed-roughened surface impinged by arrays of impinging elliptic jets have been measured by using a transient liquid crystal technique. The effects of the exit flow orientation, angled-rib arrangements, and jet Reynolds number on the characteristics of the heat transfer are

examined in detailed. It is found that the crossflow effect is closely related to the flow length experienced by the fluids after impingement. In the case of single exit, the upstream fluid travels a length near the length of the channel. For the two-exit cases, however, the fluids diverted to the both ends of the impingement channel. The short length of the development retains high transport rates in the thermal flow. The downstream peaks are diminished for increasing crossflow effect. Relatively to the heat transfer on the smooth surface, the heat transfer over the ribbed-surface may be enhanced or retarded. It is found that among the test angled-rib arrangements, the best heat transfer performance is obtained with a surface with 45° V-type ribs. In addition, the surface with continuous ribs provides a better heat transfer than that with broken ribs.

Acknowledgment

The financial support of this study by the National Science Council of Taiwan, R.O.C., through the grant number NSC 93-2212-E211-011, is gratefully acknowledged.

References

[1] A.M. Huber, R. Viskanta, Effects of jet–jet spacing on convective heat transfer to confined, impinging arrays of axisymmetric air jets, Int. J. Heat Mass Transfer 37 (1994) 2859–2869.

[2] L.W. Florschuetz, C.P. Truman, D.E. Metzger, Streamwise flow and heat transfer distribution for jet impingement with crossflow, ASME J. Heat Transfer 103 (1981) 337–342.

[3] K. Garrett, B.W. Webb, The effect of drainage configuration on heat transfer under an impinging liquid jet array, ASME J. Heat Transfer 121 (1999) 803–810.

[4] V.J.H. Lienhard, Liquid jet Impingement, in: C.L. Tien (Ed.), Annual Review of Heat Transfer, vol. 6, Begell House, New York, 1995, pp. 199–270.

[5] V. Treuren, K.W. Wang, Z. Ireland, T.V. Jones, Detailed measurements of local heat transfer coefficient and adiabatic wall temperature beneath an array of impingement jets, ASME J. Turbomachinery 116 (1994) 369–374.

[6] Y. Huang, S.V. Ekkad, J.C. Han, Detailed heat transfer distributions under an array of orthogonal impinging jets, AIAA J. Thermophys. Heat Transfer 12 (1998) 73–79.

[7] G.S. Azad, Y. Huang, J.C. Han, Impingement heat transfer on dimpled surfaces using a transient liquid crystal technique, AIAA J. Thermophys. Heat Transfer 14 (2) (2000) 186–193.

[8] D.H. Rhee, P.H. Yoon, H.H. Cho, Local heat/mass transfer and flow characteristics of array impinging jets with effusion holes ejecting spent air, Int. J. Heat Mass Transfer 46 (2003) 1049–1061.

[9] K. Kanokjaruvijit, R.F. Martinez-botas, Jet impingement on a dimpled surface with different cross schemes, Int. J. Heat Mass Transfer 48 (2005) 161–170.

[10] W.M. Yan, R.C. Hsieh, C.Y. Soong, Experimental study of surface-mounted obstacle effects on heat transfer enhancement by using transient liquid crystal thermography, ASME J. Heat Transfer 124 (2002) 762–769.

[11] W.M. Yan, H.C. Liu, C.Y. Soong, W.J. Yang, Experimental study of impingement heat transfer of incline and staggered jet arrays by using transient liquid crystal technique, J. Flow Visual. Image Process. 10 (2003) 119–141.

[12] W.M. Yan, H.S. Mei, H.C. Liu, C.Y. Soong, W.J. Yang, Measurement of detailed heat transfer on a surface under arrays of impinging elliptic jets by a transient liquid crystal technique, Int. J. Heat Mass Transfer 47 (2004) 5235–5245.

[13] C. Gau, C.M. Chung, Surface curvature effect on slot-air-jet impingement cooling flow and heat transfer process, ASME J. Heat Transfer 113 (1991) 858–864.

[14] C. Gau, C.C. Lee, Impingement cooling flow structure and heat transfer along rib-roughened walls, Int. J. Heat Mass Transfer 35 (1992) 3000–3020.

[15] J.C. Han, Heat transfer and friction in channels with two opposite rib-roughened walls, ASME J. Heat Transfer 106 (1984) 774–781.

[16] J.C. Han, J.S. Park, C.K. Lei, Heat transfer enhancement in channels with turbulence promoters, ASME J. Eng. Gas Turbines Power 107 (1985) 628–635.

[17] J.C. Han, P.R. Chandra, S.C. Lau, Local heat/mass transfer distributions around sharp 180° turns in two-pass smooth and rib-roughened channels, ASME J. Heat Transfer 110 (1988) 91–98.

[18] S.C. Lau, R.D. McMillin, J.C. Han, Heat transfer characteristics of turbulent flow in a square channel with angled discrete ribs, ASME J. Turbomachinery 113 (1991) 367–374.

[19] J.C. Han, Y.M. Zhang, High performance heat transfer ducts with parallel broken and V-shaped broken ribs, Int. J. Heat Mass Transfer 35 (1992) 513–523.

[20] W.M. Yan, H.C. Liu, C.Y. Soong, W.J. Yang, Experimental study of impinging heat transfer along rib-roughened walls by using transient liquid crystal technique, Int. J. Heat Mass Transfer 48 (2005) 2420–2428.